Proceedings of the ASME 2007 International Design Engineering Technical Conferences & Computers and Information in Engineering Conference
IDETC/CIE 2007
September 4-7, 2007, Las Vegas, Nevada, USA

DETC2007-34921

ON THE COUPLING BETWEEN TORSIONAL AND LATERAL VIBRATIONS IN A ROTOR DYNAMIC SYSTEM WITH SET-VALUED FRICTION

N. van de Wouw
H. Nijmeijer
Eindhoven University of Technology,
Department of Mechanical Engineering,
P.O. Box 513, 5600 MB Eindhoven, The Netherlands,
N.v.d.wouw@tue.nl

N. Mihajlović*
Philips Research Laboratories,
High tech Campus 34,
5656 AE Eindhoven,
The Netherlands

ABSTRACT

In this paper, we analyze the interaction between friction-induced vibrations and self-sustained lateral vibrations caused by mass-unbalance in an experimental rotor dynamic set-up. This study is performed on the level of both numerical and experimental bifurcation analyses. The results show that a higher level of mass-unbalance, which generally increases the lateral vibrations, can have a stabilizing effect on the torsional dynamics, i.e. friction-induced limit cycling can disappear. Moreover, the analyses provide insight in the fundamental mechanisms causing self-sustained oscillations in rotor systems with flexibility, mass-unbalance and discontinuous friction which supports the design of such flexible rotor systems.

INTRODUCTION

Rotating machinery such as turbines, pumps and fans are important components in e.g. aircraft engines, power stations and large flywheels in hybrid transmissions of cars. The behaviour of these rotor-dynamic components can influence the performance of the system as a whole. Namely, for certain ranges of the rotational speed, such systems can exhibit various types of vibration which can be so violent that they can cause significant damage or be performance limiting factors. Causes for such behaviour may vary from friction or fluid forces in the bearings in which a shaft is borne and mass-unbalance in a rotor which can lead to whirling motions to flexibilities present in a system. Consequently, the dynamic behaviour of such systems can be very complex (see e.g. [1–3]).

Krauter [4] has analyzed torsional vibrations in water lubricated bearings and in [5–9] torsional vibrations in drill-string systems have been analysed. In those papers, it is concluded that torsional vibrations are caused by negative damping in the friction force in the bearings ([4]), the friction force at the contact between the bit and the borehole rotor ([5–7]) and by the friction force at the rotor ([8; 9]). Lateral vibrations induced by mass-unbalance in rotor systems have been analyzed extensively in [1; 2; 10; 11].

The interaction between torsional and lateral vibrations in rotor systems is studied in [1–3; 12]. In various mechanical systems it is noticed that the increase of the mass-unbalance can have both stabilizing and destabilizing effects. In [1] and [2], a simple disc with a mass-unbalance connected to a shaft, which is elastic in both torsional and lateral direction, is considered. In such systems, under certain conditions, instabilities can appear if the unbalance increases. On the other hand, in [3; 12] the behaviour of flexible rotor-bearing systems is analyzed and it is concluded that the mass-unbalance can stabilize rotor systems.

In this paper, we focus on interaction between friction-induced torsional vibrations in flexible mechanical systems and lateral vibrations in rotor systems caused by a mass-unbalance. When analyzing the friction-induced vibrations a discontinuous

*This work was done while working at the TU/e.

static model for the friction is used. The discontinuity will have significant consequences for the analysis of the steady-state behaviour of the system. The occurrence, prediction and analysis of limit-cycling behaviour (vibrations) in systems with discontinuities is currently receiving wide attention see e.g. [6; 13–19]. However, most authors are studying such systems from a theoretical point of view. Therefore, the focus of this paper is on an experimental study of such system.

In the next section, the rotor set-up is described and the model is given. Subsequently, the system dynamics are analyzed. The focus of the analysis is on the steady-state behaviour of the system. Herein, torsional vibrations, lateral vibrations and the interaction between those vibrations in flexible rotor systems with discontinuous friction are modelled and analyzed. As a result of such analysis appropriate bifurcation diagrams are constructed. This analysis is aiming at an improved understanding of the cause of friction-induced limit cycling and effects of the interaction between the torsional and lateral dynamics that influence this type of limit cycling. Next, we compare bifurcation diagrams based on the estimated model to experimentally obtained bifurcation diagrams. We also discuss the experimental results obtained for various mass-unbalance levels. This paper is finished with conclusions.

MODEL OF THE EXPERIMENTAL SET-UP

The experimental set-up consists of a power amplifier, a DC-motor, two rotational (upper and lower) discs, a low-stiffness string and an additional brake applied to the lower disc, see Figure 1. The input voltage u is fed to the DC-motor via the power amplifier. The motor is connected, via the gear box, to the upper steel disc. The upper disc and the lower disc are connected through a low stiffness steel string. The lower disc can rotate around its geometric center and is free to move in lateral directions.

In order to induce torsional vibrations at the lower disc, a brake and a small oil-box (with ondina oil 68) with felt stripes are fixed to the upper bearing housing of the lower part of the set-up (see Figure 2). The brake produces a friction force exerted on the brake disc. The brake contact material is bronze. The steel brake disc is connected to the lower brass disc via a stiff shaft. Lateral vibrations are induced by fixing an additional mass at the lower brass disc (Figure 2). Consequently, a mass-unbalance is introduced to the disc which leads to motions in the lateral plane (whirl type motion). Tilting of the lower disc is avoided by means of two constraints; one in x- and one in y-direction, see Figure 2 and [2].

The angular positions of the upper and lower disc (θ_u and θ_l, respectively in Figure 1(b)) are measured using incremental encoders. The angular velocities of both discs are obtained by numerical differentiation of the angular positions and filtering the resulting signals using a low-pass filter with a cut-off frequency of $200\,\mathrm{rad/s}$ $(31.8\,\mathrm{Hz})$. The displacements of the geometric center of the lower disc in x- and y-directions are measured with two LVDT (Linear Variable Differential Transformer) displacement sensors. The displacement sensors measure, in fact, the displacements of the rigid bodies of the constraints in x- and y-direction which equal the displacements of the lower disc in those two directions.

The Euler-Lagrange equations are used to construct an eighth-dimensional model. The model of the set-up is derived in the co-rotating coordinate frame which is fixed to the upper disc as shown in Figure 3(b).

The dynamics of the set-up is independent of the angular position of the discs (θ_u and θ_l), but only depends on the difference $\alpha = \theta_l - \theta_u$ between these two angular positions, see Figure 3. Therefore, we replace $\dot{\theta}_u$ with ω_u, $\dot{\theta}_l$ with ω_l and after performing some equivalent transformations to the obtained dynamic model, the following seventh-order system of differential equations can be obtained:

$$J_u\dot{\omega}_u - k_\theta\alpha + T_{fu}(\omega_u) = k_m u, \tag{1}$$

$$\begin{aligned}
&(m_r+m_t)\ddot{x} - m_r e\,\ddot{\alpha}\sin(\alpha) - (m_r+m_t)\dot{\omega}_u y - m_r e\,\dot{\omega}_u\sin(\alpha) + b\dot{x}\\
&-2(m_r+m_t)\omega_u\dot{y} - 2\,m_r e\,\omega_u\,\dot{\alpha}\cos(\alpha) - m_r e\,\dot{\alpha}^2\cos(\alpha) + kx\\
&-(m_r+m_t)\omega_u^2 x - b\,\omega_u y - m_r e\,\omega_u^2\cos(\alpha) = 0,
\end{aligned}$$

$$\begin{aligned}
&(m_r+m_t)\ddot{y} + m_r e\,\ddot{\alpha}\cos(\alpha) + (m_r+m_t)\dot{\omega}_u x + m_r e\,\dot{\omega}_u\cos(\alpha) + b\dot{y}\\
&+2(m_r+m_t)\omega_u\dot{x} - 2\,m_r e\,\omega_u\dot{\alpha}\sin(\alpha) - m_r e\,\dot{\alpha}^2\sin(\alpha) + ky\\
&-(m_r+m_t)\omega_u^2 y + b\,\omega_u x - m_r e\,\omega_u^2\sin(\alpha) = 0,
\end{aligned}$$

$$\begin{aligned}
&-m_r\ddot{x}e\sin(\alpha) + m_r\ddot{y}e\cos(\alpha) + (m_r e^2 + J_C)(\ddot{\alpha}+\dot{\omega}_u) +\\
&m_r\dot{\omega}_u e(x\cos(\alpha) + y\sin(\alpha)) + 2\,m_r e\,\dot{x}\,\omega_u\cos(\alpha) + 2\,m_r e\,\dot{y}\,\omega_u\sin(\alpha)\\
&+T_{fl}(\omega_u+\dot{\alpha}) + m_r x e\,\omega_u^2\sin(\alpha) - m_r y e\,\omega_u^2\cos(\alpha) + k_\theta\alpha = 0,
\end{aligned}$$

$$T_{fu}(\omega_u) \in \begin{cases} T_{cu}(\omega_u)\mathrm{sgn}(\omega_u) & \text{for } \omega_u \neq 0,\\ [-T_{su}+\triangle T_{su},\, T_{su}+\triangle T_{su}] & \text{for } \omega_u = 0,\end{cases}$$

$$T_{cu}(\omega_u) = T_{su} + \triangle T_{su}\mathrm{sgn}(\omega_u) + b_u|\omega_u| + \triangle b_u\omega_u,$$

$$T_{fl}(\omega_l) \in \begin{cases} T_{cl}(\omega_l)\mathrm{sgn}(\omega_l) & \text{for } \omega_l \neq 0,\\ [-T_{sl},\, T_{sl}] & \text{for } \omega_l = 0,\end{cases}$$

$$T_{cl}(\omega_l) = T_{cl} + (T_{sl}-T_{cl})e^{-|\omega_l/\omega_{sl}|^{\delta_{sl}}} + b_l|\omega_l|,$$

where $\omega_l = \omega_u + \dot{\alpha}$. In (1), $T_{fu}(\omega_u)$ represents the friction torque at the upper disc caused by friction in the bearings of the upper disc and by the electro-magnetic effect in the DC-motor. Furthermore, $T_{fl}(\omega_l)$ is the friction torque at the lower disc comprising the friction in the bearings of the lower disc and the friction induced by the brake mechanism. The friction torques $T_{fu}(\omega_u)$ and $T_{fl}(\omega_l)$ are modelled using set-valued force laws. Consequently, the model of the system represents a set of differential inclusions.

In order to analyze the dynamics of the experimental set-up, we need to estimate the parameters in (1). Parameter estimation is performed using a nonlinear least-squares technique. For the sake of brevity, we only present the results here; see [2] for details on the identification procedure. In (1), $J_u = 0.4765\,\mathrm{kg\,m^2}$,

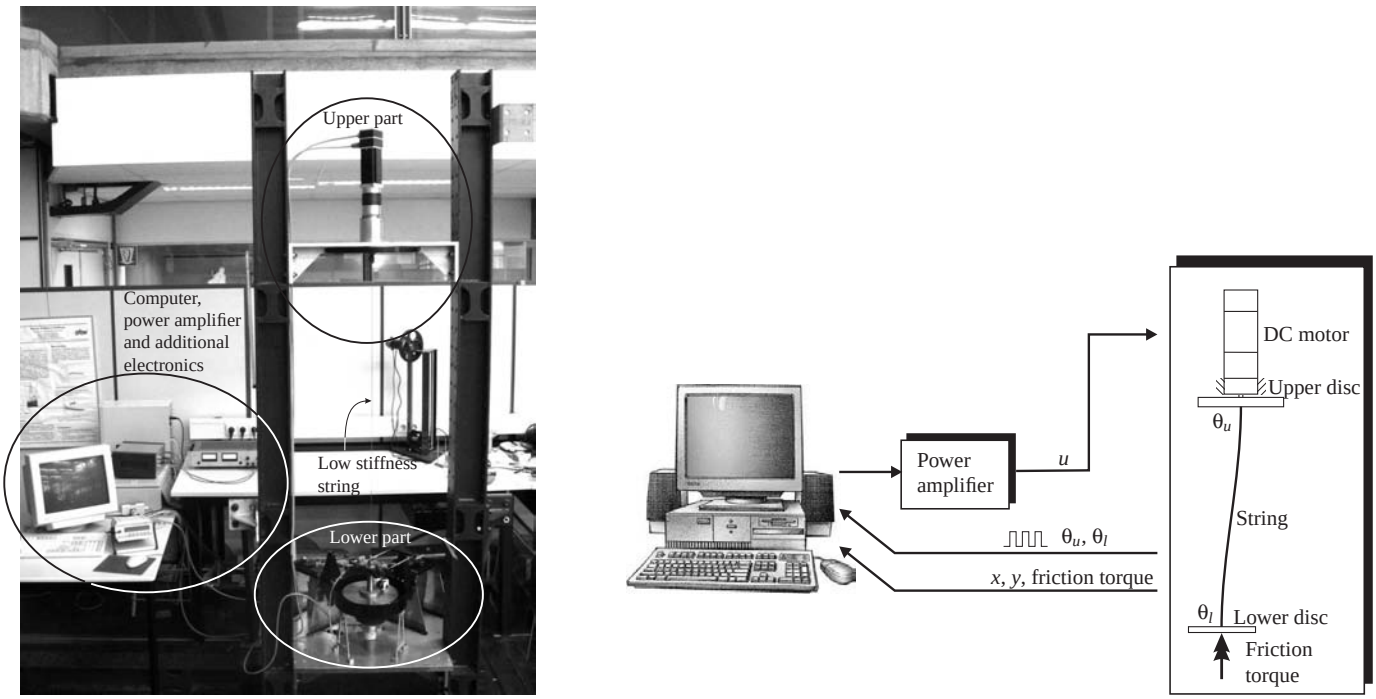

(a) Photo. (b) Schematic representation.

Figure 1. Experimental set-up.

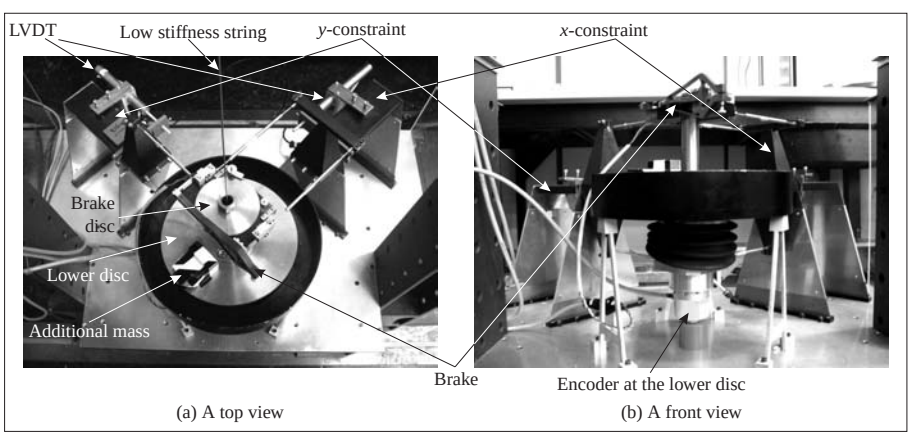

(a) A top view (b) A front view

Figure 2. The lower part of the experimental set-up.

$J_C = 0.0412\ \mathrm{kg\,m^2}$ represent the moments of inertia of the upper disc and lower discs, respectively, with respect to their centers of mass, $k_m = 4.3228\ \mathrm{N\,m/V}$ is the motor constant, $T_{su} + \triangle T_{su}$ and $-T_{su} + \triangle T_{su}$ are the maximum and minimum value of $T_{fu}(\omega_u)$ for $\omega_u = 0$ (with $T_{su} = 0.37975\ \mathrm{N\,m}$, $\triangle T_{su} = -0.00575\ \mathrm{N\,m}$). Moreover, $b_u + \triangle b_u$ and $b_u - \triangle b_u$ are the viscous friction coefficients for positive and negative velocity ω_u (with $b_u = 2.4245\ \mathrm{kg\,m^2/rad\,s}$ and $\triangle b_u = -0.0084\ \mathrm{kg\,m^2/rad\,s}$), $k_\theta = 0.0775\ \mathrm{N\,m/rad}$ is the torsional stiffness coefficient, $e = 0.00489$ m is the distance between the center of mass of the lower disc and its geometric center, $m_r = 9.9137$ kg represents the mass of all parts of the lower part of the set-up that can rotate around the geometric center of the disc, $m_t = 3.3202$ kg represents the mass of all parts of the lower part of the set-up, that do not rotate around the center of the disc but move in the same (x or y) direction during motion of the lower disc (i.e. one constraint, the brake, the oil box, the upper bearing housing, the lower bearing housing and the encoder at the lower disc).

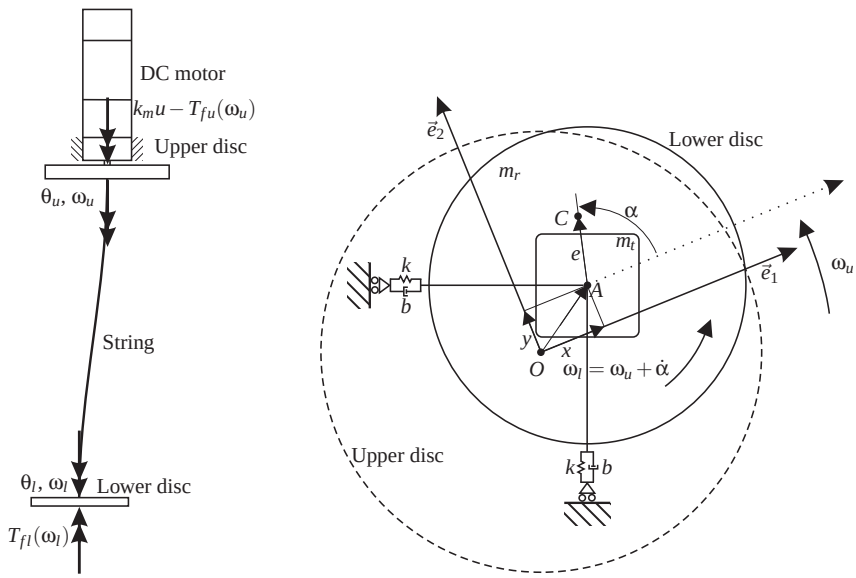

(a) The model of the set-up.

(b) The lower part of the system and the co-rotating coordinate frame $\{\vec{e}_1, \vec{e}_2\}$.

Figure 3. The rotor dynamic system.

Finally, $k = 2974.25$ N s/m is the bending stiffness coefficient in lateral direction, $b = 25$ N s/m is the damping coefficient in lateral direction, $T_{sl} = 0.2781$ N m is the static friction torque, $T_{cl} = 0.0473$ N m the Coulomb friction torque, $\omega_{sl} = 1.4302$ rad/s the Stribeck velocity and $\delta_{sl} = 2.0575$ rad/s the Stribeck shape parameter in $T_{fl}(\omega_l)$ and $b_l = 0.0105$ kg m^2/rad s is the viscous friction coefficient at the lower disc. The estimated friction torques are shown in Figure 4. From (1) and Figure 4(b) it can be seen that a negative damping is present at the friction torque at the lower disc for low angular velocities.

ANALYSIS OF NONLINEAR DYNAMIC BEHAVIOUR

When both the upper and lower disc rotate with a constant angular velocity, a forward whirling motion is performed by the lower disc (lateral vibrations) and this represents an equilibrium point in the co-rotating coordinate frame. Moreover, when torsional vibrations appear in the system, then such motion represents a periodic motion in the co-rotating coordinate frame. Therefore, both equilibrium points (sets), limit cycles and the related stability properties are analyzed.

Equilibria and Related Stability Analysis

In the equilibria, $(\omega_u, \alpha, x, y) = (\omega_{eq}, \alpha_{eq}, x_{eq}, y_{eq})$ and $\dot{\omega}_u = \ddot{\alpha} = \dot{\alpha} = \ddot{x} = \dot{x} = \ddot{y} = \dot{y} = 0$, for $u = u_c$, with u_c a constant. Clearly, $\omega_l = \omega_{eq}$ in equilibrium. According to (1), in an equilibrium the following holds:

$$k_m u_c - T_{fu}(\omega_{eq}) - T_{fl}(\omega_{eq}) - \frac{b e^2 m_r^2 \omega_{eq}^5}{(m_r + m_t)^2 \omega_{eq}^4 + b^2 \omega_{eq}^2 - 2k(m_r + m_t)\omega_{eq}^2 + k^2} = 0, \quad (2)$$

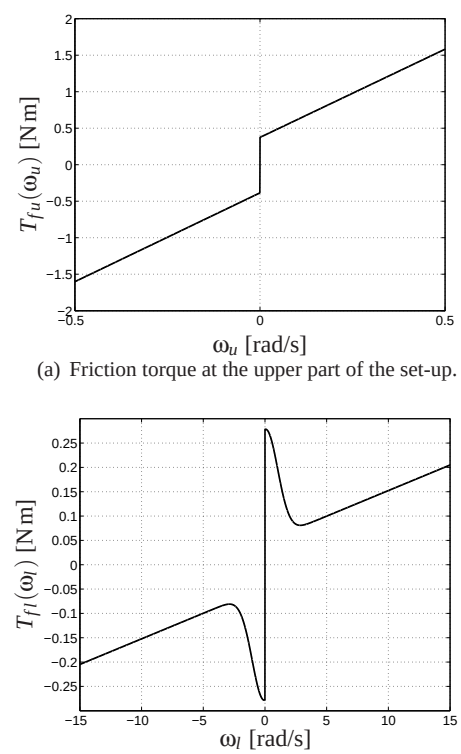

(a) Friction torque at the upper part of the set-up.

(b) Friction torque at the lower part of the set-up.

Figure 4. Estimated friction models.

$$\alpha_{eq} = -\frac{T_{fl}(\omega_{eq})}{k_\theta} - \frac{b\,e^2 m_r^2 \omega_{eq}^5}{k_\theta((m_r+m_t)^2\omega_{eq}^4 + b^2\omega_{eq}^2 - 2\,k(m_r+m_t)\omega_{eq}^2 + k^2)}, \tag{3}$$

and

$$x_{eq} = e\,m_r\omega_{eq}^2 \frac{(k-(m_r+m_t)\omega_{eq}^2)\cos(\alpha_{eq}) + b\,\omega_{eq}\sin(\alpha_{eq})}{(m_r+m_t)^2\omega_{eq}^4 + b^2\omega_{eq}^2 - 2\,k(m_r+m_t)\omega_{eq}^2 + k^2},$$

$$y_{eq} = e\,m_r\omega_{eq}^2 \frac{(k-(m_r+m_t)\omega_{eq}^2)\sin(\alpha_{eq}) - b\,\omega_{eq}\cos(\alpha_{eq})}{(m_r+m_t)^2\omega_{eq}^4 + b^2\omega_{eq}^2 - 2\,k(m_r+m_t)\omega_{eq}^2 + k^2}. \tag{4}$$

Since friction torques $T_{fu}(\omega_u)$ and $T_{fl}(\omega_l)$ are modelled using set-valued friction models, (2) and (3) represent algebraic inclusions and the following situations should be considered: firstly, equilibria for $\omega_{eq} > 0$, i.e. both the upper and the lower disc rotate with the same constant angular velocity ω_{eq} and, secondly, equilibria for $\omega_{eq} = 0$, i.e. both the upper and the lower disc stand still. For $\omega_{eq} > 0$, $T_{fu}(\omega_{eq}) = T_{cu}(\omega_{eq})$ and $T_{fl}(\omega_{eq}) = T_{cl}(\omega_{eq})$ (see (1)). Consequently, such an equilibrium point satisfies the algebraic equations

$$\begin{aligned} k_m\ u_c - (T_{su} + \triangle T_{su}) - (b_u + \triangle b_u)\omega_{eq} - T_{cl}(\omega_{eq}) \\ - \frac{b\,e^2 m_r^2 \omega_{eq}^5}{(m_r+m_t)^2\omega_{eq}^4 + b^2\omega_{eq}^2 - 2\,k(m_r+m_t)\omega_{eq}^2 + k^2} = 0, \\ \alpha_{eq} = -\frac{T_{cl}(\omega_{eq})}{k_\theta} \\ - \frac{b\,e^2 m_r^2 \omega_{eq}^5}{k_\theta((m_r+m_t)^2\omega_{eq}^4 + b^2\omega_{eq}^2 - 2\,k(m_r+m_t)\omega_{eq}^2 + k^2)}, \end{aligned} \tag{5}$$

and (4). From (1), the first equation of (5) and due to the fact that $\omega_{eq} > 0$, it can be concluded that the system has such an isolated equilibrium point when

$$u_c > u_{\mathcal{E}p} := \frac{T_{su} + \triangle T_{su} + T_{sl}}{k_m}. \tag{6}$$

For $0 \le u_c \le u_{\mathcal{E}p}$, an equilibrium set in which $\omega_{eq} = x_{eq} = y_{eq} = 0$ exists, see [2]. For the estimated parameters of the model the system has a *unique* isolated equilibrium for $u_c > u_{\mathcal{E}p}$, see [2].

Since in the set-up both torsional and lateral vibrations appear, we are interested in the angular velocity ω_l and radial displacement r of the lower disc in steady state for different constant input voltages u_c. When $u_c > u_{\mathcal{E}p}$, $\omega_l = \omega_u = \omega_{eq}$ in steady state can be obtained by solving the first equation in (5). The corresponding radial displacement of the center of the lower disc (in equilibrium) $r_{eq} = \sqrt{x_{eq}^2 + y_{eq}^2}$ can be derived from (4) as:

$$r_{eq} = \frac{m_r e\,\omega_{eq}^2}{\sqrt{(m_r+m_t)^2\omega_{eq}^4 + b^2\omega_{eq}^2 - 2\,k(m_r+m_t)\omega_{eq}^2 + k^2}}, \tag{7}$$

since $(m_r+m_t)^2\omega_{eq}^4 + b^2\omega_{eq}^2 - 2\,k(m_r+m_t)\omega_{eq}^2 + k^2 > 0$ for every $\omega_{eq} \in \mathbb{R}$ for the estimated parameters of the set-up.

In order to obtain local stability conditions for the isolated equilibrium points (for $\omega_{eq} \neq 0$), we can use Lyapunov's indirect method. The method can be only be applied when $\omega_{eq} > 0$ (i.e. condition (6) should be satisfied). Therefore, the model of system (1) is linearized around the equilibrium point and the stability of the linear model is analyzed. The results of such analysis are shown in the sequel.

Bifurcation Diagram (Nominal Case)

Since in the set-up both torsional and lateral vibrations appear, we are interested in the angular velocity ω_l and radial displacement r of the lower disc in steady-state for different constant input voltages u_c. More specifically, two bifurcation diagrams (for ω_l and r) are constructed, with u_c as a bifurcation parameter for the estimated parameters given on page 3 and 4. The equilibria are discussed in the previous section. Limit cycles are obtained numerically using a path following technique in combination with a shooting method [20]. Herein, the so-called switch model [18] is used to properly deal with the discontinuities in the dynamics, related to the set-valued nature of the friction models.

The results of an extensive bifurcation analysis are shown in the bifurcation diagrams in Figures 5 and 6. In those figures, the maximal and minimal values of ω_l and r are plotted when a limit cycle is found. The Floquet multipliers, corresponding to these limit cycles, are computed numerically and used to determine the local stability properties of these limit cycles.

For $0 < u_c \le u_{\mathcal{E}p}$, with $u_{\mathcal{E}p}$ given by (6) (point A in Figure 6), the system in steady state is in the stick phase, i.e. the system has a locally asymptotically stable equilibrium set (equilibrium branch e_1 in Figure 6), see [2] for a detailed stability argument.

For $u_c = u_{\mathcal{E}p}$ (point A in the bifurcation diagrams) the locally asymptotically stable equilibrium set reduces to a locally asymptotically stable isolated equilibrium point and no change of stability properties occurs. The system has a unique equilibrium point for $u_c > u_{\mathcal{E}p}$. Moreover, a locally asymptotically stable equilibrium branch e_2 appears (Figure 6), for which ω_{eq} and r_{eq} increase for increasing u_c.

From bifurcation point B an unstable equilibrium branch e_3 and an unstable periodic branch p_1 arise (see Figure 6). At that point a pair of complex conjugate eigenvalues, related to the linearisation of (1) around the equilibrium point, cross the imagi-

nary axis. Therefore, a smooth subcritical Hopf bifurcation occurs at point B.

The unstable periodic branch p_1 occurs for input voltages smaller than the input voltage at point B. The branch p_1 is connected to a locally stable periodic branch p_2 at the point D (u_c at point D is smaller than u_c at the point B), which represents a discontinuous fold bifurcation point, since the periodic branch p_2 consists of stable limit cycles which represent torsional vibrations with stick-slip (see Figure 6(a)). Moreover, a Floquet multiplier crosses through the point +1 in the complex plane.

For some higher constant input voltage u_c (point E in Figure 5) the locally stable periodic branch p_2 loses stability and an unstable periodic branch appears (periodic branch p_3 in Figure 5) through another discontinuous fold bifurcation (point E in Figure 5).

The unstable periodic branch p_3 is connected to the unstable equilibrium branch e_3 and the stable equilibrium branch e_4 in the smooth subcritical Hopf bifurcation point C.

For input voltages u_c higher than that at point E, the asymptotically stable equilibrium branch continues. For increasing u_c the steady-state velocity at the lower disc ω_l increases. Note that for such high angular velocities, viscous friction is dominant in the friction at the lower disc (see the estimated friction torque $T_{fl}(\omega_l)$ in Figure 4(b)), which induces the local stability of the equilibrium branch e_4.

The bifurcation diagram shown in Figure 5 also shows various branches of steady-state solutions for input voltages $u_c > 5\,\mathrm{V}$, which is in fact outside the working region of the experimental set-up. However, a rich variety of interesting qualitative changes in the dynamic behaviour can appear for those voltages; for a detailed bifurcation analysis, see [2]. The friction-induced vibrations, occurring for $u_c \in [0\,\mathrm{V},\ 3.6\,\mathrm{V}]$, are discussed in more detail in the next section.

Friction-Induced Vibrations

The vibrations, observed for $u_c \in [0\,\mathrm{V},\ 3.6\,\mathrm{V}]$, are induced by friction. Such vibrations are analyzed in more detail in [9] when the lower disc is fixed in lateral direction. The main cause for lateral vibrations is the presence of the mass-unbalance. Moreover, it appears that this mass-unbalance also affects the friction-induced torsional limit-cycling. Therefore, we analyze the influence of the level of mass-unbalance on the steady-state behaviour of the system for $u_c \in [0\,\mathrm{V},\ 4\,\mathrm{V}]$.

Hereto, we add additional mass $\triangle m$ at a distance of $d_\triangle = 0.1\,\mathrm{m}$ from the center of the lower disc in the direction of the already existing unbalance. Consequently, the parameters e, m_r and J_C of the estimated model (see page 3 and 4) are changed and the new related parameters $e_\triangle$, $m_{r\triangle}$ and $J_{C\triangle}$ are:

$$
\begin{aligned}
e_\triangle &= \frac{m_r e + d_\triangle \triangle m}{m_r + \triangle m}, \\
m_{r\triangle} &= m_r + \triangle m, \quad J_{C\triangle} = J_C + d_\triangle^2 \triangle m.
\end{aligned}
\tag{8}
$$

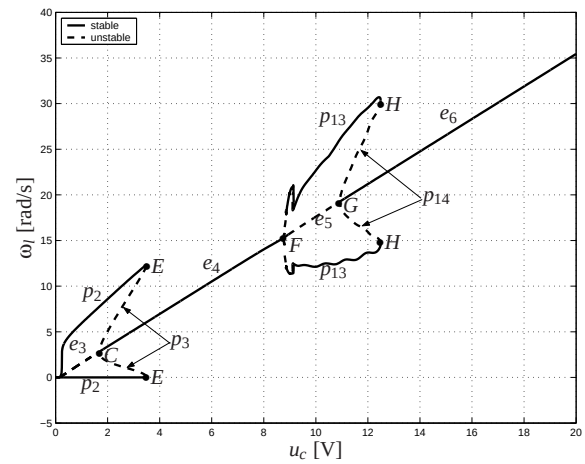

(a) Angular velocity ω_l.

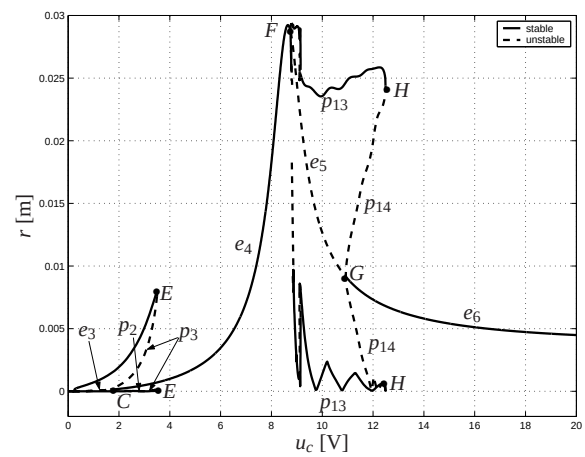

(b) Radial displacement r.

Figure 5. Bifurcation diagram of the model of the experimental set-up when both torsional and lateral vibrations are present.

In Figure 7, bifurcation diagrams are shown for the estimated system (light-grey line), for $\triangle m = 5\,\mathrm{kg}$ (dark-grey line), for $\triangle m = 50\,\mathrm{kg}$ (black line). Of course, adding an additional mass $\triangle m = 50\,\mathrm{kg}$ to the lower disc, with the estimated mass being $m_r = 9.9137\,\mathrm{kg}$, is practically impossible. However, we analyze that case in order to observe the effect of additional mass-unbalance to the steady-state behaviour of the set-up.

Due to an additional mass-unbalance, the region (in terms of the input voltage) where friction-induced torsional vibrations appear, decreases (see Figure 7(a)). Namely, if the mass-unbalance increases, the first fold and Hopf bifurcation points occur at higher input voltages. Furthermore, the second fold and Hopf bifurcation points occur at significantly lower input voltages (compare the fold bifurcation points E' and E'', and the Hopf bifurcations at C' and C'' in Figure 7(a)). Therefore, the region in which the torsional friction-induced vibrations can occur is smaller when the mass unbalance is increased. In Figure 8 we

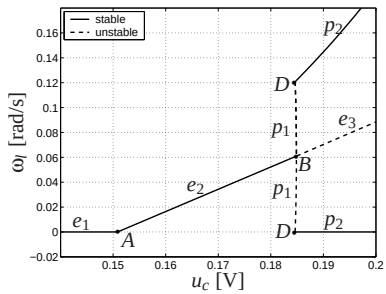

(a) Angular velocity ω_l.

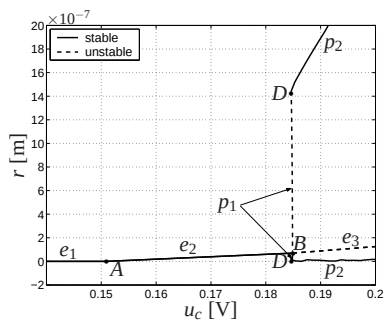

(b) Radial displacement r.

Figure 6. Bifurcation diagram as in Figure 5 for low input voltages.

present the position of the first and the second Hopf bifurcations for various levels of the added mass-unbalance, i.e. we show the region in which unstable equilibria occur for various $\triangle m$ and for $u_c \in [0\,\mathrm{V},\ 5\,\mathrm{V}]$. This figure clearly displays the influence of the level of mass unbalance on friction induced instabilities in torsional direction.

From Figure 7(b) it can be concluded that when the mass-unbalance increases, the amplitude of lateral vibrations increases both for the input voltages where torsional vibrations occur (compare periodic branch p_2' with periodic branches p_{2a}'', p_{2b}'', p_{2c}'' and p_{2d}'' in Figure 7(b)) and where no torsional vibrations appear (compare equilibrium branches e_4' and e_4'' in the same figure).

In Figure 7, we see that the periodic branch p_2', for $\triangle m = 5\,\mathrm{kg}$, splits to four branches p_{2a}'', p_{2b}'', p_{2c}'' and p_{2d}'', for $\triangle m = 50\,\mathrm{kg}$. The periodic branches p_{2a}'' and p_{2c}'' consists of torsional vibrations with stick-slip, the branch p_{2d}'' represents torsional vibrations without stick-slip. The branch p_{2b}'' represents torsional vibrations where the lower disc starts to rotate in the opposite direction during every period (i.e. $\min(\omega_l) < 0$ in a limit-cycle on p_{2b}'').

The effect of the decrease of the friction-induced torsional vibrations when the mass-unbalance is increased can be explained in the following way. When no mass-unbalance is present at the lower disc, the range in which friction-induced torsional vibrations can occur is determined by a subtle balance between negative damping at lower velocities and viscous friction at higher velocities, see [2]. Namely, the energy released

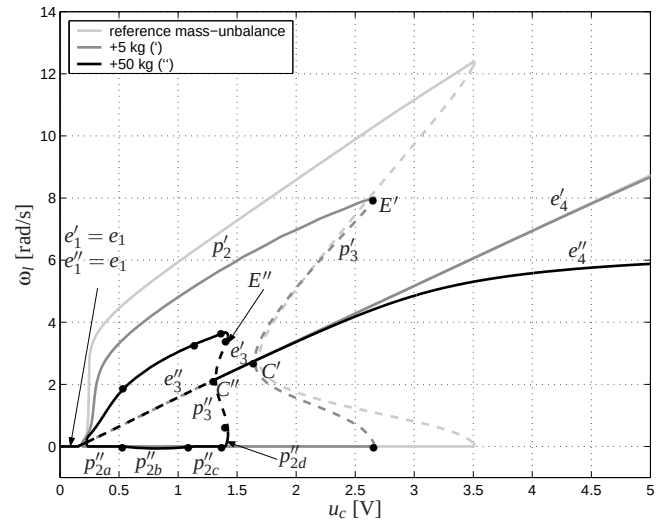

(a) Angular velocity ω_l.

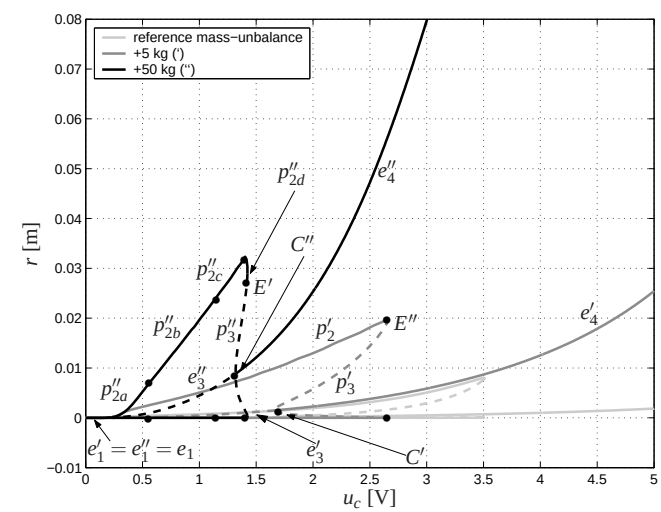

(b) Radial displacement r.

Figure 7. Bifurcation diagrams for various levels of mass-unbalance for $u_c \in [0\,\mathrm{V},\ 5\,\mathrm{V}]$.

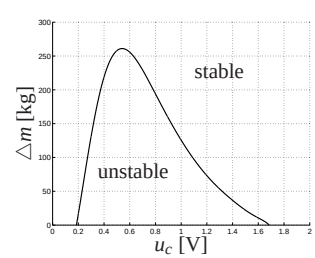

Figure 8. The regions for which the equilibrium point of the system are locally asymptotically stable and unstable.

due to the negative damping in the friction characteristics at the

lower disc is mainly transformed to kinetic energy at the lower disc (i.e. ω_l) and to the potential energy in the low-stiffness string (i.e. α) and torsional vibrations occur. When mass-unbalance is present at the lower disc, then the energy released due to the negative damping is also transformed to the potential energy stored in the leaf springs and rods (i.e. r) and kinetic energy related to the translational motion of the lower disc in lateral direction. Consequently, less energy is transformed to kinetic energy of the lower disc in torsional direction and torsional vibrations decrease. In this respect it is important to notice that, when the level of mass-unbalance is higher, the lateral vibrations increase for angular velocities which are lower than the critical angular velocity and, consequently, less energy can be transformed to kinetic energy of the disc in torsional direction. Hence, torsional vibrations decrease further or they even disappear.

EXPERIMENTAL RESULTS

Validation of Steady-State Behaviour of the Set-Up

The predictive quality of the model (1) in steady state, with the estimated parameters given on page 3 and 4, is of great interest. Therefore, a constant voltage is applied at the input of the DC motor of the set-up and each experiment lasted long enough to guarantee that all transient effects have disappeared.

Using these experiments, the same type of bifurcation diagrams, as shown in Figure 5, are constructed experimentally. However, due to limitations in the DC motor, the experimental bifurcation diagram is constructed by applying different constant input voltages in the limited voltage range $u_c \in [0\,\mathrm{V},\ 5\,\mathrm{V}]$. When no torsional vibrations are observed, the mean value of the recorded angular velocity and radial displacement are computed and the obtained data are plotted using the symbol "**x**". Next, when torsional vibrations are observed at the lower disc, the mean values of local maxima and minima of the vibrations are computed. Then, these experimentally obtained data are plotted using the symbol "**o**". Experimental results, together with the bifurcation diagram obtained by numerical analysis of the estimated model, are shown in Figures 9(a) and 9(b). Furthermore, when torsional vibrations are observed in the set-up, the period time T of the vibrations is determined as well, see Figure 9(c). The results, shown in Figure 9, illustrate the predictive quality of the obtained model.

Both in the numerical and the experimental bifurcation diagram we recognize the regions which are also present when only torsional vibrations are possible in the set-up [2; 9]: a sticking region for very low input voltages, a region in which only torsional vibrations (i.e. stable limit cycles) appear, a region in which torsional vibrations (stable limit cycles) and a constant angular velocity at the lower disc (stable equilibrium points) coexist, and a region in which no torsional vibrations can appear in steady state. For the input voltages $u_c \in [3\,\mathrm{V},\ 3.5\,\mathrm{V}]$, we notice that the estimated model is less accurate (see specifically Figure 9(b)). The reason for this fact is that some unmodelled dynamics is present

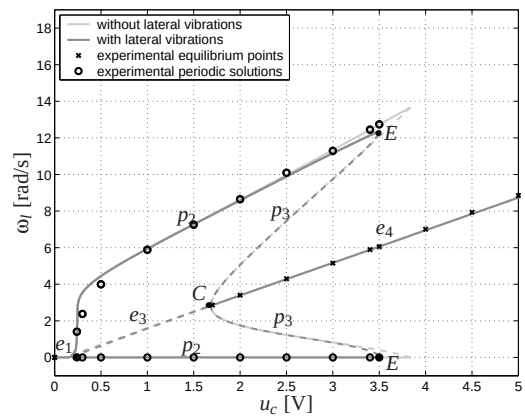

(a) Angular velocity ω_l at the lower disc.

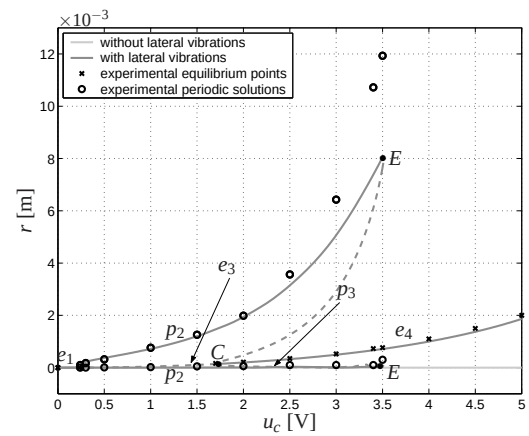

(b) Radial displacement r of the lower disc.

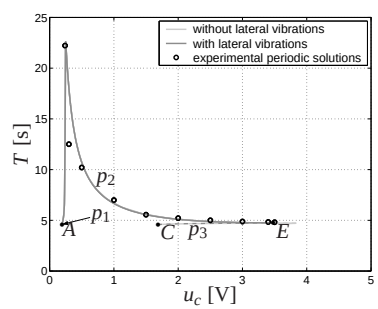

(c) Period time of the periodic solutions.

Figure 9. Comparison of the numerical and experimental bifurcation diagrams.

in the set-up such as: a position dependant friction at the lower disc, the presence of the sticking behaviour in lateral direction due to LVDT displacement sensors, see Figure 2 and anisotropic characteristics of the lower part of the set-up in lateral direction. A detailed discussion on unmodelled dynamics in the set-up is presented in [2].

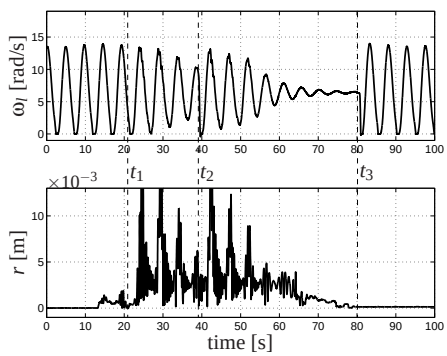

Figure 10. Indication of disappearance of torsional vibrations when the lower disc moves in lateral direction: experimental results for $u_c = 3.7\,\mathrm{V}$.

Disappearance of Torsional Vibrations

In Figure 9, with a light-grey line we show the bifurcation diagram of the set-up when only torsional and no lateral vibrations are possible, i.e. when x- and y-constraints are fixed. If we compare that bifurcation diagram with the bifurcation diagram obtained when lateral vibrations are present in the set-up (dark-grey line), we see that the second fold bifurcation point moves towards lower velocities when mass-unbalance and lateral vibrations are present in the system (as predicted in the previous section). Namely, when the constraints are fixed the second fold bifurcation point is observed for $u_c \in (3.9\,\mathrm{V},\ 4.0\mathrm{V})$ and when the constraints are released the second fold bifurcation point is observed for $u_c \in (3.5\,\mathrm{V},\ 3.6\mathrm{V})$.

In order to show that torsional vibrations can really disappear, for some voltages, due to the existence of lateral vibrations, the following experiment is performed. We fix the constraints, apply a constant input voltage of $u_c = 3.7\,\mathrm{V}$ and wait long enough to obtain torsional stick-slip vibrations (see Figure 10). Then, at time instant t_1 we release the constraints and the lower disc starts to vibrate in lateral direction. After a while, the torsional vibrations disappear even though at time instant t_2 we tried to induce those vibrations manually, by stopping the lower disc for a very short time in torsional direction. Finally, when we fix again the constraints and stop the lower disc manually (time instant t_3 in Figure 10), the system continues with stick-slip vibrations. This experiment provides additional evidence for the fact that torsional vibrations can indeed disappear due to the presence of lateral vibrations. In the next section, this effect is evidenced quantitatively in both experiments and simulations.

Bifurcation Analysis for Various Levels of Mass-Unbalance

In order to study the effect of mass-unbalance in experiments, additional masses $\triangle m = 0.6032\,\mathrm{kg}$ or $\triangle m = 1.2152\,\mathrm{kg}$ are added to the existing mass-unbalance (see Figure 2) at the following respective distances $d_\triangle$:

$$\begin{aligned} d_\triangle &= 10.85\text{ cm for } \triangle m = 0.6032\,\mathrm{kg},\text{ and} \\ d_\triangle &= 8.98\text{ cm for } \triangle m = 1.2152\,\mathrm{kg}. \end{aligned} \tag{9}$$

For both levels of mass-unbalance, model (1), (8) with parameter estimates presented as on page 3 and 4 and equation (9) the model is validated. Hereto, we construct numerical and experimental bifurcation diagrams when various constant voltages are applied at the input of the DC motor. The obtained diagrams are shown in Figure 11. The comparison between the responses of the experimental set-up and estimated model indicates the good quality of the obtained parameters for both levels of mass-unbalance. From those bifurcation diagrams, one can once more conclude that due to an additional mass-unbalance the region, in which friction-induced torsional vibrations occur (see Figure 11(a)), reduces. Namely, for $\triangle m = 0.6032\,\mathrm{kg}$ the second fold bifurcation point occurs between $u_c = 3.2\,\mathrm{V}$ and $u_c = 3.3\,\mathrm{V}$, and for $\triangle m = 1.2152\,\mathrm{kg}$ the fold bifurcation occurs between $u_c = 3.1\,\mathrm{V}$ and $u_c = 3.2\,\mathrm{V}$.

CONCLUSIONS

The aim of this paper is to provide an improved understanding on the interaction between torsional and lateral vibrations in rotor systems with flexibility, mass-unbalance and dry friction effects. For that purpose, we have analyzed an experimental rotor dynamic set-up, consisting of two discs interconnected by a low-stiffness string, in which torsional vibrations are induced by friction at the lower disc and lateral vibrations are induced by the presence of a mass-unbalance at the lower disc.

The dynamics of the set-up, described by differential inclusions (since the friction is modelled with a set-valued force law), is experimentally validated. With these differential inclusions we successfully modelled equilibrium sets, isolated equilibria and stick-slip limit cycling phenomena (and the related stability properties) also observed in the set-up. We also observe a discontinuous fold bifurcation both in simulations and experiments. Note that the experimental verification of such nonlinear phenomena, which are explicitly due to the discontinuities in the system, is relatively rare in literature.

The influence of various levels of mass-unbalance to the steady-state behaviour of the system is studied on a theoretical, numerical and experimental level. Results on all levels confirm that if the level of mass-unbalance increases, the region, in which friction-induced torsional vibrations occur, decreases. Moreover, numerical results show that if the mass-unbalance is high enough, the torsional vibrations can disappear entirely.

ACKNOWLEDGMENT

Research partially supported by European project SICONOS ($IST - 2001 - 37172$)

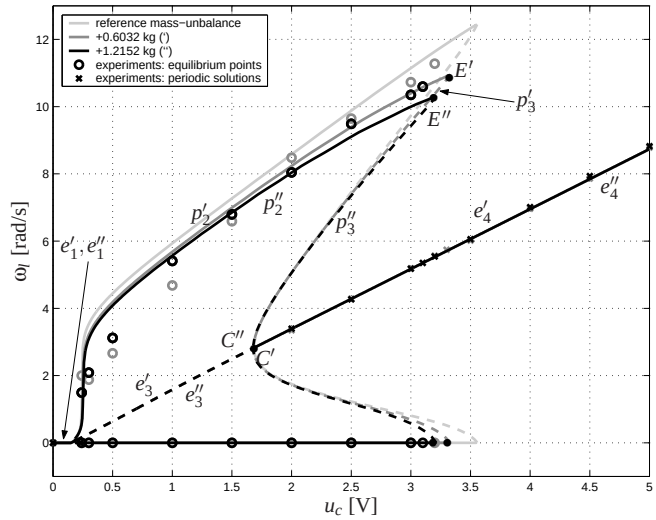

(a) Angular velocity ω_l.

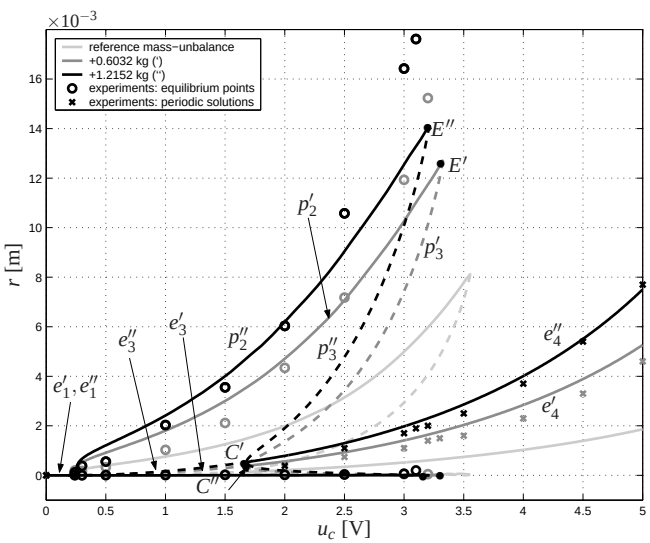

(b) Radial displacement r.

Figure 11. Simulated and experimental bifurcation diagrams for various levels of mass-unbalance applied at the lower disc.

References

[1] Chong-Won Lee. *Vibration analysis of rotors*. Kluwer Academic Publishing, Dordrecht, The Netherlands, 1993.

[2] N. Mihajlović. *Torsional and Lateral Vibrations in Flexible Rotor Systems with Friction*. PhD thesis, Eindhoven University of Technology, The Netherlands, 2005.

[3] E. L. B. Van de Vorst, R. H. B. Fey, A. De Kraker, and D. H. Van Campen. Steady-state behaviour of flexible rotor dynamics systems with oil journal bearings. In *Proc. of the ASME, Symposium on Nonlinear and Stochastic Dynamics*, volume 192, pages 107–114, New York, USA, 1994.

[4] A. I. Krauter. Generation of squeal/chatter in water-lubricated elastomeric bearings. *ASME Journal of Lubrication Technology*, 103:406–413, 1981.

[5] J. F. Brett. Genesis of torsional drillstring vibrations. *SPE Drilling Engineering*, 7(3):168–174, 1992.

[6] R. I. Leine. *Bifurcations in Discontinuous Mechanical Systems of Filippov-Type*. PhD thesis, Eindhoven University of Technology, The Netherlands, 2000.

[7] R. I. Leine, D. H. Van Campen, and W. J. G. Keultjes. Stick-slip whirl interaction in drillstring dynamics. *ASME Journal of Vibrations and Acoustics*, 124:209–220, 2002.

[8] N. Mihajlović, A. A. Van Veggel, N. Van de Wouw, and H. Nijmeijer. Analysis of friction-induced limit cycling in an experimental drill-string set-up. *ASME Journal of Dynamic Systems, Measurements and Control*, 126(4):709–720, 2004.

[9] N. Mihajlović, N. Van de Wouw, M. P. M. Hendriks, and H. Nijmeijer. Friction-induced limit cycling in flexible rotor systems: an experimental drill-string set-up. *Nonlinear Dynamics*, 6(3):273–291, 2005.

[10] R. J. Fritz. The effects of an annular fluid on the vibrations of a long rotor, part 1 - theory. *ASME Journal of Basic Engineering*, pages 923–929, 1970a.

[11] A. Muszynska. Whirl and whip - rotor/bearing stability problems. *Journal of Sound and Vibrations*, 110(3):443–462, 1986.

[12] E. J. Gunter, R. H. Humphris, and H. Springer. Influence of unbalance on the nonlinear dynamical response and stability of flexible rotor-bearing systems. *Rotor Dynamical Instability*, 115:37–58, 1983.

[13] H. Dankowitz and A. B. Nordmark. On the origin and bifurcations of stick-slip oscillations. *Physica D*, 136(3–4):280–302, 2000.

[14] M. Di Bernardo, M. I. Feigin, S. J. Hogan, and M. E. Homer. Local analysis of c-bifurcations in n-dimensional piecewise-smooth dynamical systems. *Chaos, Solutions and Fractals*, 10(11):1881–1908, 1999.

[15] U. Galvanetto, S. R. Bishop, and L. Briseghella. Event maps in a stick-slip systems. *Nonlinear Dynamics*, pages 99–115, 1997.

[16] M. Kunze and T. Küpper. Qualitative bifurcation analysis of a non-smooth friction-oscillator model. *Zeitschrift für angewandte Math. un Physik ZAMP*, 48:87–101, 1997.

[17] R. I. Leine and D. H. Van Campen. Discontinuous fold bifurcations. *Systems Analysis Modelling Simulation*, 43(3):321–332, 2003.

[18] R. I. Leine and H. Nijmeijer. *Dynamics and Bifurcations of Non-smooth Mechanical Systems*. Springer, Berlin, 2004.

[19] K. Popp and P. Stelter. Stick-slip vibrations and chaos. *Philosophical Transactions of the Royal Society of London*, 332:89–105, 1990.

[20] T. S. Parker and L. O. Chua. *Practical Numerical Algorithms for Chaotic Systems*. Springer-Verlag, 1989.